Distortion in the thermal noise spectrum and quality factor of nanomechanical devices due to finite frequency resolution with applications to the atomic force microscope

John E. Sader,[1,a)] Julian Sanelli,[2] Barry D. Hughes,[1] Jason P. Monty,[3] and Evan J. Bieske[2]
[1]*Department of Mathematics and Statistics, The University of Melbourne, Victoria 3010, Australia*
[2]*School of Chemistry, The University of Melbourne, Victoria 3010, Australia*
[3]*Department of Mechanical Engineering, The University of Melbourne, Victoria 3010, Australia*

(Received 18 April 2011; accepted 12 August 2011; published online 9 September 2011)

The thermal noise spectrum of nanomechanical devices is commonly used to characterize their mechanical properties and energy dissipation. This spectrum is measured from finite time series of Brownian motion of the device, which is windowed and Fourier transformed. Here, we present a theoretical and experimental investigation of the effect of such finite sampling on the measured device quality factor. We prove that if no spectral window is used, the thermal noise spectrum retains its original Lorentzian distribution but with a reduced quality factor, indicating an apparent enhancement in energy dissipation. A simple analytical formula is derived connecting the true and measured quality factors – this enables extraction of the true device quality factor from measured data. Common windows used to reduce spectral leakage are found to distort the (true) Lorentzian shape, potentially making fitting problematic. These findings are expected to be of particular importance for devices with high quality factors, where spectral resolution can be limited in practice. Comparison and validation using measurements on atomic force microscope cantilevers are presented. © *2011 American Institute of Physics*. [doi:10.1063/1.3632122]

I. INTRODUCTION

Transduction of environmental effects into mechanical signals underlies the operation of mechanical sensors, including cantilever devices,[1] electromechanical resonators,[2] and optical tweezers.[3] The sensitivity of these devices to external stimuli can be improved dramatically by miniaturization to the nanoscale.[4] This reduces device mass, increases resonant frequencies, and lowers device stiffness, thereby enabling detection of environmental changes with incredible sensitivity. Such capacity has most recently been demonstrated through atomic resolution mass sensing of the heavier elements using carbon nanotube resonators.[5,6] Other applications include use of nanomechanical devices in ultrasensitive force detection in the atomic force microscope (AFM),[7] and mass spectrometry of biomolecules.[8]

An ability to characterize the mechanical properties of nanomechanical devices is core to many applications and is often performed through measurement of their Brownian (thermal) fluctuations.[9–17] The power spectral density of thermal fluctuations – the thermal noise spectrum – is then used to determine mechanical properties, such as device stiffness,[9–11,14] device resonant frequencies,[16,17] and energy dissipation.[12,13] The latter property is easily discerned through measurement of the "width" of the individual resonance peaks.[1,2,4] Since many nanomechanical devices do not lend themselves to techniques used at the macroscale, the thermal noise spectrum provides a passive and highly sensitive approach for determining the mechanical and energetic properties of nanoscale devices.

Importantly, the thermal noise spectrum is determined in practice by measuring finite time series of Brownian motion of the device. This time series is then windowed to reduce spectral leakage, Fourier transformed, and averaged to obtain the required result.[18] A range of different approaches/algorithms can be used for this signal analysis, a review of which is given in Ref. 18. The frequency range of the resultant thermal noise spectrum is specified by the Nyquist frequency (half the sampling frequency), and the frequency resolution by the reciprocal of the time interval over which the sample is taken. The latter is often limited due to practical issues associated with data collection and processing. This provides a fundamental restriction on the measurement of devices with small dissipation, which inherently possess sharp resonance peaks. Unless frequency resolution is sufficiently fine, such resonance peaks can be (artificially) omitted in the measured thermal noise spectrum. Furthermore, limited frequency resolution can also lead to distortion of the measured thermal noise spectrum and problems in fitting the resonance peaks; see Ref. 18 for a general discussion of spectral distortion. This can potentially lead to a misinterpretation of the mechanical and energetic properties of nanoscale devices and uncertainty in measurements obtained from their thermal noise spectra. These effects are yet to be studied and commonly ignored in applications involving the thermal noise spectrum of nanomechanical devices, such as measurements performed using the atomic force microscope.

In this article, we examine the effect of finite frequency resolution on the measured thermal noise spectrum of nanomechanical devices. In particular, we focus on the effect of window functions that are commonly used to reduce spectral leakage.[18] Throughout, we assume a Lorentzian distribution for each resonance peak of the true thermal noise

a)Author to whom correspondence should be addressed. Electronic mail: jsader@unimelb.edu.au.

spectrum. This feature is often encountered in practice, especially for devices with high quality factors (low energy dissipation), which is the case of interest here – these devices possess sharp resonance peaks.[12] We find that if a rectangular window is used (corresponding to no window), the measured thermal noise spectrum retains its original Lorentzian distribution, but with a reduced effective quality factor:

$$Q_{\text{eff}} = Q\left(1 - \frac{Q\, f_s}{\pi\, f_0 N}\right), \tag{1}$$

where Q is the true device quality factor, f_s is the sampling frequency (Hz), f_0 is the device resonant frequency (Hz), and N is the number of elements in the time series ($N \gg 1$) – this corresponds to measurement of finite time series of length N/f_s seconds. This reduced quality factor can be misinterpreted as an enhancement in energy dissipation, but is due to an artifact introduced by finite sample size.

The simple formula in Eq. (1) enables extraction of the true device quality factor from measurement of the thermal noise spectrum. Use of windows that reduce spectral leakage is found to distort the true Lorentzian shape, making fitting and interpretation of measurements potentially problematic, as we shall discuss. These findings indicate that use of windows to reduce spectral leakage may be detrimental to the quantitative interpretation of thermal noise measurements of nanomechanical devices. To examine the practical implications of these findings, a detailed comparison to measurements on microcantilevers commonly used in the atomic force microscope is presented. Excellent agreement is observed between the derived theory and measurements.

Importantly, the findings of this study apply not only to mechanical devices, but also to a broader range of applications where Lorentzian distributions are expected. The underlying theoretical analysis is completely general and only assumes that the thermal noise spectrum is Lorentzian – no mechanical equation is used. Consequently, this study is also applicable to other practical situations, such as chemical reactions,[19] biological processes,[20] and optical phenomena,[21] where resonance phenomena are expected.

We commence with the theoretical formalism used to analyze the effects of finite frequency resolution. Rectangular and triangular windows are then studied using this theory – explicit analytical formulas are presented in both cases and Eq. (1) is derived. Next, we compare the sampled thermal noise spectrum to a Lorentzian distribution, to quantify the deviations due to finite frequency resolution. Finally, a detailed comparison of the derived theory to measurements on AFM cantilevers is presented. Mathematical details are relegated to an Appendix.

II. THEORETICAL FORMULATION

We consider a mechanical resonator whose Brownian (thermal) motion is sampled at a frequency f_s (Hz). The power spectral density (PSD) is then estimated from time series of N discrete elements of this sampled signal, which is windowed and Fourier transformed (see Ref. 18 for details). The expected value of the computed PSD is given by[18]

$$E\{P(f)\} = \frac{1}{f_s N A}\int_{-\frac{f_s}{2}}^{\frac{f_s}{2}} |W(f - f')|^2 P(f')\, df', \tag{2}$$

where $W(f)$ is the discrete Fourier transform of the window function $w(n)$ applied to the time series of length N, and A is a normalization constant that ensures the power in the expected value of the PSD is unaffected by the window choice:

$$A = \frac{1}{N}\sum_{n=0}^{N-1} |w(n)|^2. \tag{3}$$

The true PSD of an ideal damped harmonic oscillator is given by[2,7]

$$P(f) = \frac{f_0^4}{Q^2}\frac{1}{\left(f^2 - f_0^2\right)^2 + \frac{f^2 f_0^2}{Q^2}}, \tag{4}$$

where f_0 is the resonant frequency, Q is the quality factor, and the PSD has been normalized to unit power at the resonant frequency. In the limit of high quality factor Q, where Eq. (4) is formally valid in many cases of practical interest,[1,7,12,22] Eq. (4) can be simplified to give a Lorentzian function in the neighborhood of the resonant frequency $f \sim f_0$, i.e.:

$$P(f) \approx \frac{f_0^2}{4Q^2}\frac{1}{(f - f_0)^2 + \frac{f_0^2}{4Q^2}}. \tag{5}$$

This Lorentzian function is taken as the true PSD signal throughout the following analysis. Consequently, this analysis implicitly assumes high quality factors, i.e., $Q \gg 1$.

Strictly, a second Lorentzian function centered at $f = -f_0$ should be included in Eq. (5), due to symmetry in Eq. (4) for positive and negative frequencies. Due to linearity of Eq. (2), however, its inclusion is superfluous to the conclusions of the following analysis and is omitted for convenience.

We consider two window functions often used in practice: a *rectangular* and a *triangular* window – the latter is also commonly called the *Bartlett* window.[18,23] Others such as the Hanning and Hamming windows can also be studied using the following theoretical framework, but produce greater analytical complexity due to their functional forms.

The magnitude of the discrete Fourier transform of the *rectangular* window with N elements is[23]

$$|W_{\text{RECT}}(f)| = \left|\frac{\sin\left(N\pi\frac{f}{f_s}\right)}{\sin\left(\pi\frac{f}{f_s}\right)}\right|, \tag{6a}$$

whereas for a *triangular* window, it is[23]

$$|W_{\text{TRI}}(f)| = \frac{2}{N}\frac{\sin^2\left(\frac{\pi N}{2}\frac{f}{f_s}\right)}{\sin^2\left(\pi\frac{f}{f_s}\right)}. \tag{6b}$$

Note that a rectangular window is equivalent to the use of no window.

To proceed, we highlight three important features of our analysis:

(i) We are interested in the expected value of the PSD only in the immediate vicinity of the resonant frequency, f_0, where Eq. (5) attains its maximum amplitude.
(ii) Since the quality factor is large, $Q \gg 1$, the PSD in Eq. (5) is sharply peaked at the resonant frequency, f_0.
(iii) Because a large sample size ($N \gg 1$) is required in practice for a meaningful estimate of the spectral density, the discrete Fourier transform of the window function, W, will also be sharply peaked in the vicinity of its origin, i.e., where its argument is zero.

It then follows that both the discrete Fourier transform of the window function, W, and the PSD, P, in Eq. (2) are sharply peaked and closely spaced in the frequency domain. Consequently, the dominant contribution from $W(f - f')$ in Eq. (2) comes from frequencies in the immediate vicinity of its origin, where it attains its maximum value, i.e., $f' \sim f_0$. This corresponds to the small frequency limit of $W(f)$ in Eqs. (6), i.e., $f \ll f_0 < f_s$.

As such, the denominators of Eqs. (6) can be accurately represented by their linear approximations, i.e., $\sin(\pi f/f_s) \approx \pi f/f_s$. Importantly, the same approximation cannot be used for the numerators of Eqs. (6), because a large sample size ($N \gg 1$) ensures that these numerators vary strongly with frequency. The discrete Fourier transforms of the window functions in Eqs. (6) are therefore well approximated by

$$|W(f)| = \frac{N}{M}\left|\mathrm{sinc}^M\left(\frac{N\pi}{M}\frac{f}{f_s}\right)\right|, \tag{7}$$

where as usual $\mathrm{sinc}\, x \equiv x^{-1}\sin x$ and

$$M = \begin{cases} 1: \text{ Rectangular window} \\ \\ 2: \text{ Triangular window} \end{cases}. \tag{8}$$

We also note that in the limit, $N \to \infty$, the normalization constants for these windows are

$$A = \begin{cases} 1: \quad \text{Rectangular window} \\ \\ 1/3: \quad \text{Triangular window} \end{cases}. \tag{9}$$

Substituting Eqs. (5), (7), and (9) into Eq. (2) yields

$$E\{P(f)\} = \frac{f_0^2}{4Q^2}\frac{3^{M-1}N}{M^2 f_s}\int_{-\frac{f_s}{2}}^{\frac{f_s}{2}} \frac{\mathrm{sinc}^{2M}\left(\frac{N\pi}{M}\frac{f-f'}{f_s}\right)}{(f'-f_0)^2 + \frac{f_0^2}{4Q^2}}\, df'. \tag{10}$$

Through a simple change of variable, and noting that the quality factor Q is large, we obtain

$$E\{P(f_0+\Delta f)\} = \frac{3^{M-1}\alpha}{\pi M^2} \times \int_{-\infty}^{\infty} \frac{\mathrm{sinc}^{2M}\left(\frac{1}{M}\left[\alpha g - \pi N\frac{\Delta f}{f_s}\right]\right)}{g^2+1}\, dg, \tag{11}$$

where $f \equiv f_0 + \Delta f$, and the dimensionless parameter α is defined as

$$\alpha = \frac{\pi N f_0}{2Q f_s}, \tag{12a}$$

which is proportional to the number of discrete frequency divisions in the vicinity of the resonance peak; note that this dimensionless parameter appears in Eq. (1). For convenience, we identify and define another dimensionless variable in Eq. (11),

$$\beta \equiv \pi N\frac{\Delta f}{f_s}, \tag{12b}$$

which is proportional to the ratio of frequency deviation Δf from resonance to the frequency division f_s/N in $E\{P(f)\}$.

The integral defined in Eq. (11) can be evaluated using contour integration (see the Appendix),

$$E_{\mathrm{RECT}}\{P(f_0+\Delta f)\} = \frac{\alpha^2}{\alpha^2+\beta^2} + \frac{\alpha}{2(\alpha^2+\beta^2)^2} \times \{(\beta^2-\alpha^2)[1-e^{-2\alpha}\cos(2\beta)] - 2\alpha\beta\, e^{-2\alpha}\sin(2\beta)\}, \tag{13a}$$

$$E_{\mathrm{TRI}}\{P(f_0+\Delta f)\} = \frac{\alpha^2}{\alpha^2+\beta^2} + \frac{3\alpha^2(3\beta^2-\alpha^2)}{(\alpha^2+\beta^2)^3} + \frac{3\alpha}{2(\alpha^2+\beta^2)^4}\{(\alpha^4-6\alpha^2\beta^2+\beta^4) \times [3-4e^{-\alpha}\cos\beta + e^{-2\alpha}\cos(2\beta)] + 4\alpha\beta\,(\alpha^2-\beta^2)[4e^{-\alpha}\sin\beta - e^{-2\alpha} \times \sin(2\beta)]\}. \tag{13b}$$

For large α, i.e., large number of frequency divisions in vicinity of the resonance peak, the exponentially small terms can be ignored to leading order, yielding

$$E_{\mathrm{RECT}}\{P(f_0+\Delta f)\} = \frac{1}{1+\tau^2}\left\{1+\frac{1}{2\alpha}\frac{\tau^2-1}{(1+\tau^2)}\right\}, \tag{14a}$$

$$E_{\mathrm{TRI}}\{P(f_0+\Delta f)\} = \frac{1}{1+\tau^2}\left\{1+\frac{3}{\alpha^2}\frac{3\tau^2-1}{(1+\tau^2)^2} + \frac{9}{2\alpha^3}\frac{(1-6\tau^2+\tau^4)}{(1+\tau^2)^3}\right\}, \tag{14b}$$

where

$$\tau = \frac{\beta}{\alpha} = \frac{2Q\Delta f}{f_0}. \tag{15}$$

We therefore observe that in the limit, $\alpha \to \infty$, i.e., infinite number of (discrete) frequency divisions in the vicinity of the resonance peak, we recover the original Lorentzian distribution from Eqs. (11) and (14),

$$E\{P(f_0+\Delta f)\} = \frac{1}{1+\tau^2} = \frac{1}{1+\left(\frac{2Q\Delta f}{f_0}\right)^2}, \tag{16}$$

for both windows, as required; note that Eqs. (5) and (16) are identical.

Therefore, the bracketed terms in Eqs. (14) provide multiplicative distortions to the original Lorentzian distribution,

due to (discrete) sampling effects. The nature of these distortions depends on the choice of the window, which is examined in Sec. II A.

A. Distortion to original Lorentzian distribution

To begin, we rewrite Eqs. (14) in their (exact) infinite power series expansions:

$$E_{\mathrm{RECT}}\{P(f_0+\Delta f)\} = \sum_{n=0}^{\infty}(-1)^n\left[1-\frac{2n+1}{2\alpha}\right]\tau^{2n}, \tag{17a}$$

$$E_{\mathrm{TRI}}\{P(f_0+\Delta f)\} = \sum_{n=0}^{\infty}(-1)^n\left[1-\frac{3(n+1)(2n+1)}{\alpha^2} + \frac{3(n+1)(2n+1)(2n+3)}{2\alpha^3}\right]\tau^{2n}. \tag{17b}$$

Note that the integral of each expression over all frequencies is independent of α, as evident from Eq. (2). Next, we manipulate Eqs. (17) to investigate the effects of each window on the PSD.

1. Rectangular window

First, the magnitude of the PSD for a rectangular window at resonance, i.e., $\tau = 0$, is extracted from the summation in Eq. (17a), i.e.,

$$E_{\mathrm{RECT}}\{P(f_0+\Delta f)\} = \left(1-\frac{1}{2\alpha}\right)\sum_{n=0}^{\infty}(-1)^n \times\left[\frac{1-\frac{2n+1}{2\alpha}}{1-\frac{1}{2\alpha}}\right]\tau^{2n}. \tag{18}$$

Use of a binomial expansion then yields

$$E_{\mathrm{RECT}}\{P(f_0+\Delta f)\} = \left(1-\frac{1}{2\alpha}\right)\sum_{n=0}^{\infty}(-1)^n \times\left[1-\frac{1}{2\alpha}+O\left(\frac{1}{\alpha^2}\right)\right]^{2n}\tau^{2n}, \tag{19}$$

which immediately gives

$$E_{\mathrm{RECT}}\{P(f_0+\Delta f)\} = \frac{1-\frac{1}{2\alpha}}{1+\left[1-\frac{1}{2\alpha}+O\left(\frac{1}{\alpha^2}\right)\right]^2\tau^2}. \tag{20}$$

Substituting Eq. (15) into Eq. (20) gives the required leading order result (for large α):

$$E_{\mathrm{RECT}}\{P(f_0+\Delta f)\} = \frac{1-\frac{1}{2\alpha}}{1+\left(\frac{2Q_{\mathrm{eff}}\Delta f}{f_0}\right)^2}, \tag{21}$$

where

$$Q_{\mathrm{eff}} = Q\left(1-\frac{1}{2\alpha}\right) = Q\left(1-\frac{Q f_s}{\pi N f_0}\right). \tag{22}$$

Equations (21) and (22) establish that use of a rectangular window maintains a Lorentzian PSD distribution, with a reduced effective quality factor, Q_{eff}; all formulas have been derived for $N \gg 1$. Note that f_s/N is the frequency division from the discrete Fourier transform, whereas $\pi f_0/Q$ is the "width" of the resonance peak. As such, the term $Q f_s/(\pi N f_0) = (f_s/N)/(\pi f_0/Q)$ in Eq. (22) must be much smaller than unity to enable the resonance peak to be observed. This, in turn, ensures that the right hand side of Eq. (22) is never negative in practice.

The forms of Eqs. (21) and (22) are consistent with the asymptotic behavior of Eq. (14a),

$$E_{\mathrm{RECT}}\{P(f_0+\Delta f)\} = \begin{cases} 1-\frac{1}{2\alpha} & :\tau \ll 1 \\ \left(1+\frac{1}{2\alpha}\right)\frac{1}{\tau^2} & :\tau \gg 1 \end{cases}, \tag{23}$$

showing that a decrease in α produces a decrease in magnitude at resonance ($\tau = 0$) and a commensurate increase at large τ. Since the integral of the PSD over all frequencies is independent of α (see Eq. (2)), such flattening of the PSD is in line with a reduction in its effective quality factor.

2. Triangular window

The complexity of the summed term in Eq. (17b) (for a triangular window) does not permit a similar analysis to that performed for the rectangular window. To gain insight into the form of the PSD for a triangular window, we thus examine the asymptotic limits of small and large τ. From Eqs. (14b), we find

$$E_{\mathrm{TRI}}\{P(f_0+\Delta f)\} = \begin{cases} 1-\frac{3}{\alpha^2}+\frac{9}{2\alpha^3} & :\tau \ll 1 \\ \frac{1}{\tau^2} & :\tau \gg 1 \end{cases}. \tag{24}$$

Since (i) the asymptotic form for small τ depends on α, whereas that for large τ is independent of α, and (ii) the integral of the PSD over all frequencies is independent of α, Eq. (24) establishes that the PSD for a triangular window is not compatible with a Lorentzian response under a modified quality factor. Use of a triangular window will thus distort the PSD away from a Lorentzian response, in contrast to the behavior for a rectangular window.

Since a Lorentzian function is normally assumed in measuring and fitting the PSD of nanomechanical devices, this finding has significant implications in practice. This will be examined further in Sec. II B, where a detailed numerical comparison to a Lorentzian response is presented.

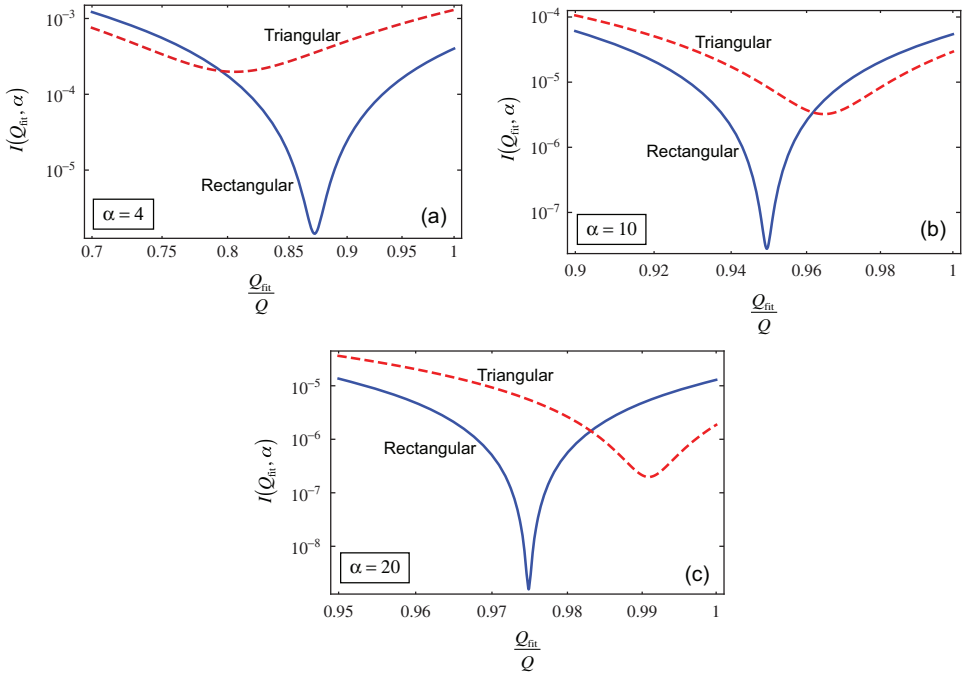

FIG. 1. (Color online) Mean square difference between expected values of PSD for rectangular (blue solid line) and triangular (red dashed line) windows, and Lorentzian distribution as a function of adjustable quality factor, $Q_{\rm fit}$; see Eq. (25). (a) $\alpha = 4$; Eq. (22) yields $Q_{\rm eff}/Q = 0.875$; (b) $\alpha = 10$; Eq. (22) yields $Q_{\rm eff}/Q = 0.95$; (c) $\alpha = 20$; Eq. (22) yields $Q_{\rm eff}/Q = 0.975$.

B. Comparison to modified Lorentzian distribution

In this section, we investigate numerically the distortion of the original Lorentzian distribution, as a function of sample size, i.e., as the dimensionless parameter α is varied. Since the above analysis and conclusions were performed under the assumption of large α, we restrict our discussion to such values.

To quantitatively assess distortions away from a Lorentzian distribution, we calculate the integrated mean square difference between Eqs. (14) and a Lorentzian with an adjustable quality factor, $Q_{\rm fit}$, i.e.,

$$I\left(Q_{\rm fit},\ \alpha\right) = \int_{-\infty}^{\infty} \left[\bar{E}\left\{P\left(f\right)\right\} - P_{\rm fit}\left(f \mid Q_{\rm fit}\right)\right]^2 df, \tag{25}$$

where

$$P_{\rm fit}\left(f \mid Q_{\rm fit}\right) = \frac{f_0^2}{4Q_{\rm fit}^2} \frac{1}{\left(f - f_0\right)^2 + \frac{f_0^2}{4Q_{\rm fit}^2}} \tag{26}$$

and $\bar{E}\left\{P\left(f\right)\right\} = E\left\{P\left(f\right)\right\}/E\left\{P\left(f_0\right)\right\}$.

Since both $\bar{E}\left\{P\left(f\right)\right\}$ and $P_{\rm fit}\left(f \mid Q_{\rm fit}\right)$ are normalized to unity at resonance, $I\left(Q_{\rm fit},\ \alpha\right)$ gives a measure of the overall distortion in $\bar{E}\left\{P\left(f\right)\right\}$ away from a Lorentzian distribution. This is calculated as a function of the adjustable quality factor $Q_{\rm fit}$ and the discretization parameter α.

In Fig. 1, we present results for $I\left(Q_{\rm fit},\ \alpha\right)$, for three values of α. Note that $I\left(Q_{\rm fit},\ \alpha\right)$ exhibits minima as $Q_{\rm fit}$ is varied, and the positions of these minima differ for rectangular and triangular windows. The values of $Q_{\rm fit}$ where minima occur decrease with decreasing α. Also noteworthy is that the magnitudes of $I\left(Q_{\rm fit},\ \alpha\right)$ at these minima are two orders of magnitude smaller for the rectangular window than those for the triangular window – demonstrating that rectangular windows enable much more precise fits. This finding is in complete agreement with the above theoretical analysis showing that a rectangular window maintains the original Lorentzian distribution, albeit with a reduced quality factor.

Predictions from Eq. (22) for the effective quality factor (under a rectangular window) are also given in the caption of Fig. 1, and are in good agreement with the positions of the observed minima in $I\left(Q_{\rm fit},\ \alpha\right)$; note that Eq. (22) is derived in the asymptotic limit $\alpha \gg 1$, and yields results that deviate by less than 1% from these minima.

Interestingly, the triangular window exhibits a minimum at a larger effective quality factor, for higher values of α; see Figs. 1(b) and 1(c). This is also expected since distortions in the PSD for a triangular window are $O(1/\alpha^2)$, whereas those for a rectangular window are $O(1/\alpha)$. For the lowest values of α (see Fig. 1(a)), the triangular window possesses a minimum at a lower effective quality factor than that for the rectangular window. The reason for this behavior is evident from Eq. (24), where the leading order correction for finite α has a large numerical coefficient. Thus, while the correction is $O(1/\alpha^2)$ for the triangular window, it can be significant for smaller α. From Fig. 1, it is clear that the Lorentzian function produces a much better fit when a rectangular window is used – a triangular window yields a PSD that deviates more strongly from Lorentzian; this is investigated further below.

To illustrate these deviations graphically, Fig. 2 presents a comparison of (i) the original Lorentzian PSD distribution, Eq. (5), (ii) the expected values of the PSD, Eq. (14), and (iii) the fitted Lorentzians yielding minima in $I\left(Q_{\rm fit},\ \alpha\right)$. From Fig. 2, it is immediately evident that a rectangular window produces a PSD that very closely approximates a Lorentzian function, whereas significant deviations are observed for a triangular window. Even though the rectangular

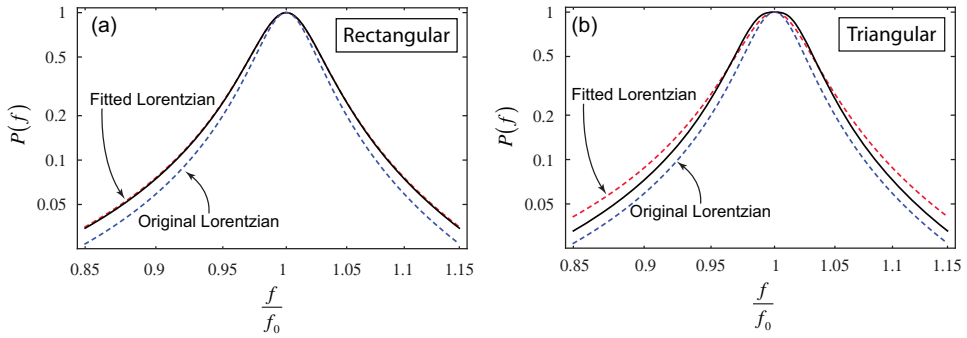

FIG. 2. (Color online) PSD of original Eq. (5) (lower dashed line), windowed Eq. (14) (solid line), and fitted Lorentzian (upper dashed line) for $\alpha = 4$. (a) Rectangular window; (b) Triangular window.

window broadens the response more significantly, it can be accurately fit to a Lorentzian function – the true quality factor can then be determined using Eq. (22).

The above findings are of significant importance in practice, since they clearly establish that triangular windows can degrade the precision of fits to a Lorentzian function, with commensurate inaccuracies in the resulting quality factors. This is especially problematic at lower values of α, where such deviations are accentuated.

Moderately small values of α can be easily encountered in practice using devices with high quality factors, e.g., measurements in vacuum.[12] Our study therefore indicates that use of rectangular windows and the correction formula in Eq. (22) may be preferable to ensure precise fits to a Lorentzian function and accurate measured quality factors. Use of rectangular windows also allows for the largest range in α to be probed experimentally.

III. EXPERIMENTAL COMPARISON

In this section, we present a detailed comparison of the above theoretical results to experimental measurements on AFM cantilevers. Three cantilevers were chosen for this purpose, and their quality factors were adjusted by varying the surrounding gas pressure. This allows for great tunability of the thermal noise spectra, and a comprehensive comparison to theory. The device specifications are listed in Table I, including their nominal resonant frequencies in air (1 atm) and spring constants.

Importantly, the theoretical analysis and results in Sec. II are independent of the specific type of device (or cantilever) – the only assumption is that the true response exhibits Lorentzian behavior. This feature will be assessed in the following discussion.

Each cantilever listed in Table I was placed separately into a specially designed vacuum chamber fitted with a glass window, housing only the cantilever. The chamber was evacuated through a vacuum line, and results were obtained for four pressures: 100, 200, 400, and 760 Torr (1 atm). Nitrogen gas was used throughout, although the specific gas used has no bearing on the comparison to theory. This procedure gave 12 cantilever-gas pressure combinations. A HeNe laser beam (Thorlabs 633 nm, 1.5 mW) was focused with a 60 mm focal length lens onto the back of the cantilever tip and the reflected spot was detected using a quadrant photodiode (OSI Optoelectronics), allowing measurement of the cantilever deflection. The photodiode output was amplified and passed through a bandpass filter, where low- and high-frequency noise away from the cantilever resonance was attenuated. The resulting signal was fed into a data acquisition DAQ board (Data Translation DT9832–04-2-BNC, 16-bit), and a digital fast Fourier transform was calculated for each time-series acquisition using MATLAB software. Specifically, a long (60 s) time series sample was collected in each case, which was subdivided, windowed, and Fourier transformed. The power spectral density was calculated directly from the discrete Fourier transform of each non-overlapping subdivision (burst), which was subsequently averaged to yield the final result.[18] This allowed variation of the time-series burst size and type of window.

Fitted measurements of the quality factor of Cantilever A in 1 atm N_2 are presented in Fig. 3, as a function of the discretization parameter α. This was achieved by fitting the measured PSD to a Lorentzian function using the peak amplitude, resonant frequency, and quality factor as parameters.[24] Rectangular, triangular, and Hanning windows were used in determination of the thermal noise spectra. From Fig. 3, it is evident that the measured quality factor decreases with decreasing α. Notably, the extracted quality factors decrease

TABLE I. List of cantilevers used in experimental comparison, together with their specifications, fundamental resonant frequencies f_0 in air (1 atm), and spring constants k.

Cantilever	Model	Shape	Length (μm)	Width (μm)	f_0 (kHz)	k (N/m)
A	NanoWorld Arrow TL1	Rectangular	500	100	6	0.03
B	Veeco MLCT-O10 Lever D	Triangular	220	22	15	0.03
C	Veeco MLCT-O10 Lever E	Triangular	140	18	38	0.1

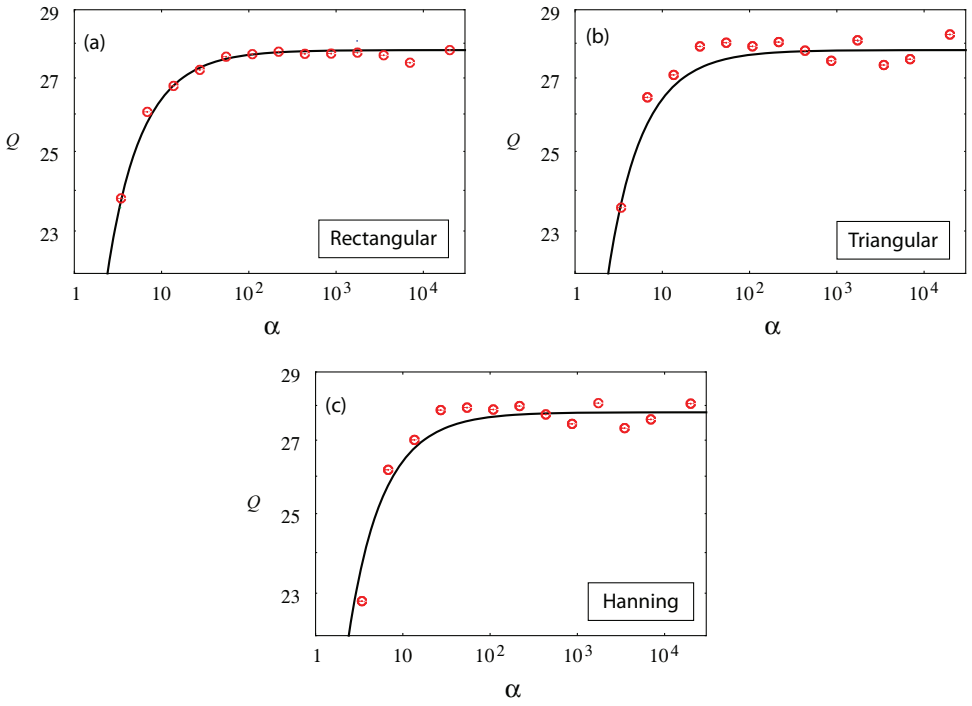

FIG. 3. (Color online) Plot of measured quality factor (dots) as a function of discretization parameter α for Cantilever A at 1 atm N_2. Analysis performed using (a) rectangular, (b) triangular, and (c) Hanning windows. Solid line is the prediction from Eq. (22) for a rectangular window.

more rapidly for the rectangular window, also as predicted – more scatter is observed for the triangular and Hanning windows. These results demonstrate that spectral distortion does indeed lead to a reduction in the measured quality factors.

To assess the level of distortion due to different window functions, a comparison of the thermal noise spectra and their fits to Lorentzians is given in Fig. 4, for a moderately small value of α. This is again performed for rectangular, triangular, and Hanning windows, and includes values for the extracted quality factors. Figure 4 clearly demonstrates that only the rectangular window yields good fits to the measured thermal noise spectrum, with significant distortion occurring for the triangular and Hanning windows. In all cases, we again find that the fitted quality factors underestimate the (true) measured value at high α, which is found to be $Q = 27.8$. While all windows give similar values for the fitted quality factors, the poorer fits to the Hanning and triangular windowed data may be contributing to this finding; window choice is expected to modify the spectral distortion.

Next, we assess the universal validity of Eq. (22), which enables the true quality factor to be determined from the measured value. Importantly, this formula is derived for rectangular windows only. For this assessment, all three cantilevers were measured over a range of different pressures and their thermal noise spectra were determined as a function of time series burst size, i.e., various α. As discussed, a single time series measurement of 60 s duration was taken for each cantilever-gas pressure combination, and subsequently analyzed as a function of burst size (i.e., α) and window function. The "true value" for the quality factor Q_∞ in each case was taken to be its value at the largest α, where the whole

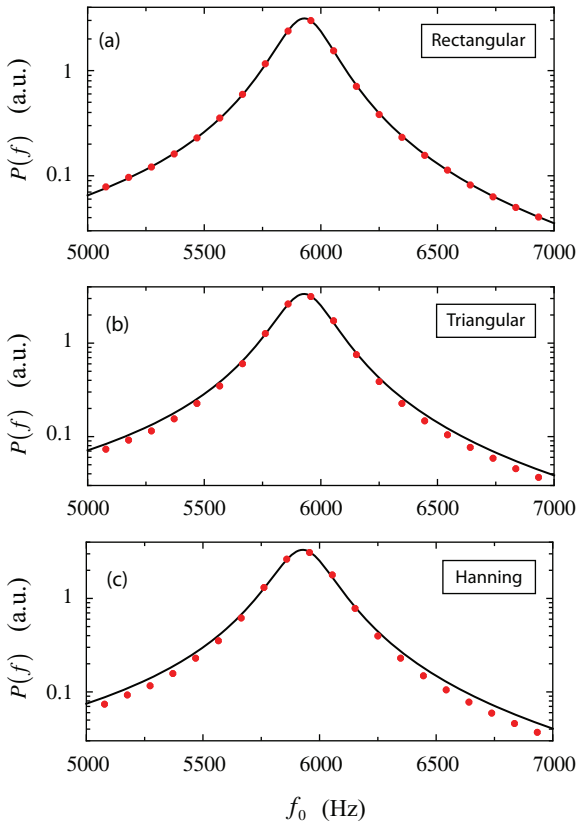

FIG. 4. (Color online) Comparison of measured thermal noise spectra (dots) of Cantilever A at 1 atm N_2 for $\alpha = 3.4$, and their corresponding fits to a Lorentzian function. (a) Rectangular window, $Q_{\text{fit}} = 23.8$; (b) Triangular window, $Q_{\text{fit}} = 23.6$; (c) Hanning window, $Q_{\text{fit}} = 22.8$. Fitted value for large α: $Q_\infty = 27.8$

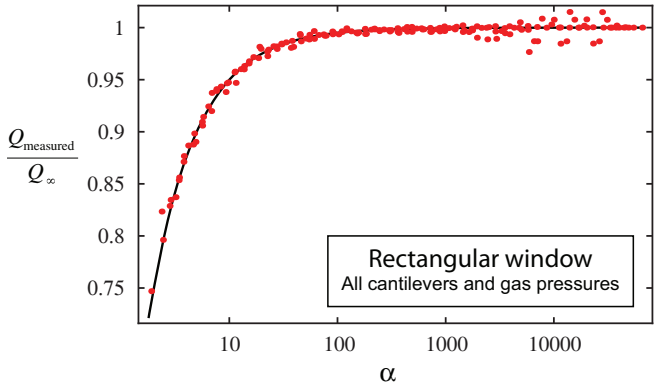

FIG. 5. (Color online) Plot of $Q_{\text{measured}}/Q_\infty$ (dots) as a function of α for all cantilever-gas pressure combinations. Thermal noise spectra determined using a rectangular window. Theoretical curve (solid line) is Eq. (22).

60 s measured time series was used in evaluation of the power spectral density. For each cantilever-gas pressure combination, the measured quality factors were then normalized by this value.

Figure 5 presents results for all cantilever-gas pressure combinations, when a rectangular window is used in determination of the thermal noise spectra. Also shown is the prediction of Eq. (22), which is found to predict the experimental data accurately in all cases. We emphasize that this comparison involves 12 cantilever-gas pressure combinations. Excellent agreement between theory and measurement is observed in all cases, which strongly supports the validity of Eq. (22). The observed scatter in the measured quality factor as $\alpha \to \infty$ is most likely due to a significant fraction of the 60 s data being discarded in evaluation of the power spectral densities.

This finding enables the true quality factor of any device to be determined at arbitrary frequency discretization through inversion of Eq. (22), i.e.,

$$Q = \frac{\pi f_0}{2\delta f}\left(1 - \sqrt{1 - Q_{\text{eff}}\frac{4\delta f}{\pi f_0}}\right), \tag{27}$$

where Q is the true quality factor, f_0 and Q_{eff} are the measured (fitted) resonant frequency and quality factor, respectively, and $\delta f \equiv f_s/N$ is the frequency division from the discrete Fourier transform, i.e., the frequency division in the thermal noise spectrum; $N \gg 1$ is implicitly assumed, which is the practical case.

In Fig. 6, we present analogous results for the triangular and Hanning windows, where we observe a similar reduction in the measured quality factor with decreasing α. Interestingly, while the data appears to follow a similar trend to that observed for the rectangular window, more scatter is evident in the data. This may, in part, be due to these windows distorting the thermal noise spectrum from its true Lorentzian response, yielding greater variability in the fits and hence the extracted quality factors. We note, however, that the predicted resonance peaks will be close to Lorentzian, since the α parameter is large in many cases. Nonetheless, this does appear to have a significant influence in fits, with the rectangular window only giving tight fitted values for the quality factors; this is consistent with the theoretical results in Fig. 1.

The findings of this article are especially significant for measurements performed in ultra high vacuum, for which microcantilevers typically exhibit very high quality factors, e.g., ~10 000–100 000, or higher.[12] Limitations in instrumentation electronics mean that frequency resolution may be restricted in many practical cases,[12] resulting in potential problems for extracting the true quality factor of devices. This study establishes that if rectangular windows are used, the true quality factor can be immediately evaluated from the measured apparent quality factor, using Eq. (27). The presence of a true Lorentzian in measurements, when rectangular windows are used, also facilitates fitting and thus measurement accuracy.

IV. CONCLUSIONS

We have examined the effect of finite time sample size and the use of window functions on the measured thermal noise spectra of devices. It was found that the measured quality factor, and hence energy dissipation, can be strongly affected by these parameters. Rectangular windows retain the true Lorentzian distribution of the device, albeit with a reduced quality factor. A simple analytical formula was derived

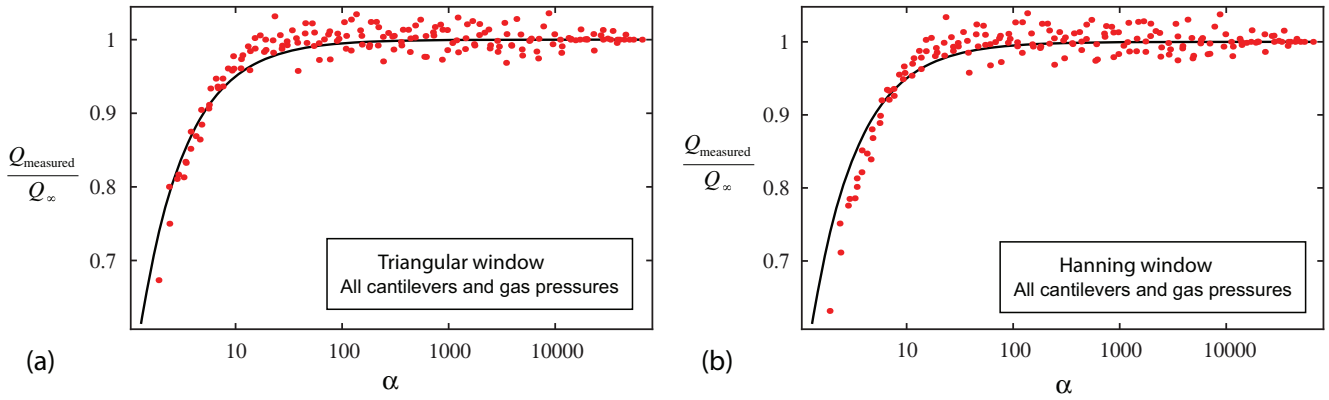

FIG. 6. (Color online) Plot of $Q_{\text{measured}}/Q_\infty$ (dots) as a function of α for all cantilever-gas pressure combinations. Thermal noise spectra determined using (a) triangular window and (b) Hanning window. Theoretical curve (solid line) is Eq. (22).

allowing for extraction of the true quality factor from the measured value, Eq. (27). This formula is solely dependent on the frequency resolution in the discrete Fourier transform and the resonant frequency of the device. Windows that reduce spectral leakage, such as triangular and Hanning windows, were found to distort the Lorentzian distribution making fitting potentially problematic. A detailed comparison to experimental measurements on AFM cantilevers was presented to examine the validity of the theoretical findings, for which excellent agreement was found.

ACKNOWLEDGMENTS

The authors would like to thank Ivan Marusic and Paul Mulvaney for useful discussions and access to equipment, and Jason Kilpatrick for experimental data. This research was supported by the Australian Research Council Grants Scheme.

APPENDIX: INTEGRAL EVALUATION

In this Appendix, we evaluate the integrals in Eq. (11) for $M = 1$ and $M = 2$ using contour integration. These cases correspond to use of rectangular and triangular windows, respectively.

Consider the integral in Eq. (11):

$$I_M = \int_{-\infty}^{\infty} \frac{\operatorname{sinc}^{2M}\left(\frac{1}{M}[\alpha x - \beta]\right)}{x^2+1} dx = \int_{-\infty}^{\infty} \frac{\sin^{2M}\left(\frac{1}{M}[\alpha x - \beta]\right)}{\left(\frac{1}{M}[\alpha x - \beta]\right)^{2M}(x^2+1)} dx. \tag{A1}$$

In evaluating Eq. (A1) by contour integral methods, indented contours are used to avoid a singularity that arises at β/α.

1. Case 1

For $M = 1$, corresponding to use of a rectangular window, Eq. (A1) becomes

$$I_1 = \int_{-\infty}^{\infty} \frac{1 - \cos(2[\alpha x - \beta])}{2(\alpha x - \beta)^2 (x^2+1)} dx. \tag{A2}$$

If we replace the cosine by a complex exponential, the imaginary part of the integrand becomes singular at $x = \beta/\alpha$; however, we have

$$I_1 = \lim_{\varepsilon \to 0} \operatorname{Re}\left\{ \int_{-\infty}^{\frac{\beta}{\alpha}-\varepsilon} + \int_{\frac{\beta}{\alpha}+\varepsilon}^{\infty} \frac{1 - \exp(2i[\alpha x - \beta])}{2(\alpha x - \beta)^2 (x^2+1)} dx \right\}. \tag{A3}$$

Consider the related contour integral in the complex z-plane:

$$J_1 = \operatorname{Re}\left\{ \oint_C \frac{1 - \exp(2i[\alpha z - \beta])}{2(\alpha z - \beta)^2 (z^2+1)} dz \right\}. \tag{A4}$$

The simple closed contour C in the upper half plane is traversed anticlockwise. Where ε is small and R is large, C consists of the segments $(-\infty, \beta/\alpha - \varepsilon)$ and $(\beta/\alpha + \varepsilon, \infty)$ of the real axis, the small semicircular arc $|z - \beta/\alpha| = \varepsilon$ (which we denote by S), and the great arc $|z| = R$. The only singular point enclosed by the contour C is the simple pole at $z = i$, and the residue theorem gives

$$J_1 = \frac{\pi}{2(\alpha^2+\beta^2)^2}\{(\beta^2 - \alpha^2)[1 - e^{-2\alpha}\cos(2\beta)] - 2\alpha\beta e^{-2\alpha}\sin(2\beta)\}. \tag{A5}$$

Since the contribution from the great arc $|z| = R$ vanishes in the limit $R \to \infty$, it follows that the contour integral in Eq. (A4) can be rewritten as

$$J_1 = \lim_{\varepsilon \to 0} \operatorname{Re}\left\{ \int_{-\infty}^{\frac{\beta}{\alpha}-\varepsilon} + \int_{\frac{\beta}{\alpha}+\varepsilon}^{\infty} \frac{1 - \exp(2i[\alpha x - \beta])}{2(\alpha x - \beta)^2 (x^2+1)} dx \right\} + \lim_{\varepsilon \to 0} \operatorname{Re}\left\{ \int_S \frac{1 - \exp(2i[\alpha z - \beta])}{2(\alpha z - \beta)^2 (z^2+1)} dz \right\}, \tag{A6}$$

where the semicircular contour S (traversed clockwise) has been defined above. Setting $z = \beta/\alpha + \varepsilon e^{i\theta}$, we can show easily that

$$\lim_{\varepsilon \to 0} \operatorname{Re}\left\{ \int_S \frac{1 - \exp(2i[\alpha z - \beta])}{2(\alpha z - \beta)^2 (z^2+1)} dz \right\} = -\frac{\pi\alpha}{\alpha^2+\beta^2}. \tag{A7}$$

Substituting Eqs. (A3), (A5) and (A7) into Eq. (A6) gives the required result:

$$I_1 = \frac{\pi\alpha}{\alpha^2+\beta^2} + \frac{\pi}{2(\alpha^2+\beta^2)^2}\{(\beta^2 - \alpha^2)[1 - e^{-2\alpha}\cos(2\beta)] - 2\alpha\beta e^{-2\alpha}\sin(2\beta)\}. \tag{A8}$$

2. Case 2

For $M = 2$, corresponding to use of a triangular window, Eq. (A1) becomes

$$I_2 = \int_{-\infty}^{\infty} \frac{6 - 8\cos(\alpha x - \beta) + 2\cos(2[\alpha x - \beta])}{(\alpha x - \beta)^4 (x^2+1)} dx. \tag{A9}$$

Following along similar lines to the analysis of Case 1, we rewrite Eq. (A9) as

$$I_2 = \lim_{\varepsilon \to 0} \operatorname{Re}\left\{ \int_{-\infty}^{\frac{\beta}{\alpha}-\varepsilon} + \int_{\frac{\beta}{\alpha}+\varepsilon}^{\infty} \times \frac{6 - 8\exp(i[\alpha x - \beta]) + 2\exp(2i[\alpha x - \beta])}{(\alpha x - \beta)^4 (x^2+1)} dx \right\}, \tag{A10}$$

and consider the related contour integral

$$J_2 = \operatorname{Re}\left\{ \oint_C \times \frac{6 - 8\exp(i[\alpha z - \beta]) + 2\exp(2i[\alpha z - \beta])}{(\alpha z - \beta)^4 (z^2+1)} dz \right\}, \tag{A11}$$

where the contour C is as defined for Case 1. Use of the residue theorem gives

$$J_2 = \frac{2\pi}{(\alpha^2+\beta^2)^4}\{(\alpha^4 - 6\alpha^2\beta^2 + \beta^4)[3 - 4e^{-\alpha}\cos\beta + e^{-2\alpha}\cos(2\beta)] + 4\alpha\beta(\alpha^2-\beta^2)[4e^{-\alpha}\sin\beta - e^{-2\alpha} \times \sin(2\beta)]\}. \quad \text{(A12)}$$

Again, the contribution from the great arc $|z| = R$ in the upper half plane is zero, in the limit $R \to \infty$. Equation (A12) can therefore be rewritten as

$$J_2 = \lim_{\varepsilon\to 0} \mathrm{Re}\left\{\int_{-\infty}^{\frac{\beta}{\alpha}-\varepsilon} + \int_{\frac{\beta}{\alpha}+\varepsilon}^{\infty} \frac{6 - 8\exp(i[\alpha x-\beta]) + 2\exp(2i[\alpha x-\beta])}{(\alpha x-\beta)^4(x^2+1)}dx\right\} + \lim_{\varepsilon\to 0}\mathrm{Re}\left\{\int_S \frac{6 - 8\exp(i[\alpha z-\beta]) + 2\exp(2i[\alpha z-\beta])}{(\alpha z-\beta)^4(z^2+1)}dz\right\}. \quad \text{(A13)}$$

The contour integral in Eq. (A13) is evaluated using polar coordinates as in Case 1, giving

$$\lim_{\varepsilon\to 0}\mathrm{Re}\left\{\int_S \frac{6 - 8\exp(i[\alpha z-\beta]) + 2\exp(2i[\alpha z-\beta])}{(\alpha z-\beta)^4(z^2+1)}dz\right\} = -\frac{4\pi\alpha}{3(\alpha^2+\beta^2)} - \frac{4\pi\alpha(3\beta^2-\alpha^2)}{(\alpha^2+\beta^2)^3}. \quad \text{(A14)}$$

Substituting Eqs. (A10), (A12), and (A14) into Eq. (A13) then gives the required result:

$$I_2 = \frac{4\pi\alpha}{3(\alpha^2+\beta^2)} + \frac{4\pi\alpha(3\beta^2-\alpha^2)}{(\alpha^2+\beta^2)^3} + \frac{2\pi}{(\alpha^2+\beta^2)^4}\{(\alpha^4 - 6\alpha^2\beta^2 + \beta^4)[3 - 4e^{-\alpha}\cos\beta + e^{-2\alpha}\cos(2\beta)] + 4\alpha\beta(\alpha^2-\beta^2)[4e^{-\alpha}\sin\beta - e^{-2\alpha}\sin(2\beta)]\}. \quad \text{(A15)}$$

[1] N. V. Lavrik, M. J. Sepaniak, and P. G. Datskos, Rev. Sci. Instrum. **75**, 2229 (2004).
[2] K. L. Ekinci and M. L. Roukes, Rev. Sci. Instrum. **76**, 061101 (2005).
[3] K. C. Neuman and S. M. Block, Rev. Sci. Instrum. **75**, 2787 (2004).
[4] H. G. Craighead, Science **290**, 1532 (2000).
[5] K. Jensen, K. Kim, and A. Zettl, Nat. Nanotechnol. **3**, 533 (2008).
[6] H.-Y. Chiu, P. Hung, H. W. Ch. Postma, and M. Bockrath, Nano Lett. **8**, 4342 (2008).
[7] F. J. Giessibl, Rev. Mod. Phys. **75**, 949 (2003).
[8] A. K. Naik, M. S. Hanay, W. K. Hiebert, X. L. Feng, and M. L. Roukes, Nat. Nanotechnol. **4**, 445 (2009).
[9] J. L. Hutter and J. Bechhoefer, Rev. Sci. Instrum. **64**, 1868 (1993).
[10] J. P. Cleveland, S. Manne, D. Bocek, and P. K. Hansma, Rev. Sci. Instrum. **64**, 403 (1993).
[11] J. E. Sader, J. W. M. Chon, and P. Mulvaney, Rev. Sci. Instrum. **70**, 3967 (1999).
[12] K. Y. Yasumura, T. D. Stowe, E. M. Chow, T. Pfafman, T. W. Kenny, B. C. Stipe, and D. Rugar, J. Microelectromech. Syst. **9**, 117 (2000).
[13] M. R. Paul and M. C. Cross, Phys. Rev. Lett. **92**, 235501 (2004).
[14] J. E. Sader, J. Pacifico, C. P. Green, and P. Mulvaney, J. Appl. Phys. **97**, 124903 (2005).
[15] R. J. Clarke, O. E. Jensen, J. Billingham, A. P. Pearson, and P. M. Williams, Phys. Rev. Lett. **96**, 050801 (2006).
[16] M. Li, H. X. Tang, and M. L. Roukes, Nat. Nanotechnol. **2**, 114 (2007).
[17] T. Li, S. Kheifets, and M. G. Raizen, Nat. Phys. **7**, 527 (2011).
[18] A. V. Oppenheim, R. W. Schafer, and J. R. Buck, *Discrete-Time Signal Processing* (Prentice-Hall, Upper Saddle River, NJ, 1999).
[19] B. P. Belousov, "Oscillation reaction and its mechanism," in *Sbornik Referatov po Radiacioni Medicine* (Medgiz, Moscow, 1959), p. 145; A. M. Zhabotinskii, Dokl. Akad. Nauk SSSR **157**, 392 (1964).
[20] A. T. Winfree, J. Theor. Biol. **16**, 15 (1967).
[21] N. Hodgson and H. Weber, *Optical resonators – Fundamentals, Advanced Concepts and Applications* (Springer-Verlag, London, 1997).
[22] J. E. Sader, J. Appl. Phys. **84**, 64 (1998).
[23] F. J. Harris, Proc. IEEE **66**, 51 (1978).

[24] The power spectral density was fit to $A_{white} + A_0 f_0^4/[(f^2 - f_0^2)^2 + f^2 f_0^2/Q^2]$, where A_{white}, A_0, f_0, and Q are fitting parameters. The first term accounts for any noise sources additional to that of the device. Fits were performed in the immediate vicinity of the resonance peak.